Journal Name

ARTICLE

Fullerene-linked tetrabenzoporphyrins for solution-processed organic photovoltaics: flexible vs. rigid linkers

Received 00th January 20xx,
Accepted 00th January 20xx

DOI: 10.1039/x0xx00000x

www.rsc.org/

Yuto Tamura,[a] Daiki Kuzuhara,[a] Mitsuharu Suzuki,[a] Hironobu Hayashi,[a] Naoki Aratani,[a] and Hiroko Yamada*[,a]

Solution process of layer-by-layer structure is possible with a precursor approach, in which the soluble precursors of insoluble or low-soluble target materials are spin-coated on the substrate and are converted to insoluble semiconducting films by heating. We have tried to construct a p-i-n structure (p: p-layer; i: interlayer by a mixture of p- and n-materials; n: n-layer) by solution process. To increase the donor–acceptor interface area, we have synthesized covalently linked donor–acceptor compounds, tetrabenzoporphyrin (**BP**)–fullerene (C_{60}) dyad. To investigate the effect of covalent connection of donor and acceptor units on the film morphology and on the OPV performances, **BP** and fullerene units were connected by a flexible or rigid linker (**f-BP–C_{60}** or **r-BP–C_{60}**). To synthesize these dyads, new synthetic routes of mono-*meso*-substituted **BP**s using [2 + 2] and [2 + 1 + 1] condensation reactions were performed. The intramolecular fluorescence quenching efficiency of **BP** by C_{60} unit of **f-BP-C_{60}** was higher than that of **r-BP–C_{60}** in CH_2Cl_2 because of the flexibility of the linker and the close location of C_{60} unit to **BP** unit. The carrier mobility in **r-BP–C_{60}** film measured by space-charge-limited-current (SCLC) technique was better than that of **f-BP–C_{60}** film and bulk heterojunction (BHJ)-type OPV performance of **r-BP–C_{60}** film was also better than that of **f-BP–C_{60}** film. In spite of the better PCE performance of **r-BP–C_{60}** device than **f-BP–C_{60}**, the short circuit current (J_{SC}) and FF of the p–i–n device with **BP**, **f-BP–C_{60}**, and [6,6]-phenyl-C_{61}-butyric acid methyl ester (**PCBM**) for p-, i- and n-layers was better than the that with **r-BP–C_{60}** in i-layer. AFM image of the layers and OPV performances suggested the flexible **f-BP–C_{60}** is suitable for the i–layer on highly crystalline **BP** film, because the roughness of **BP** film is leveled by **f-BP–C_{60}** and the electric properties of the device is improved by smooth interface.

Introduction

Organic photovoltaic devices (OPVs) have attracted much attention as next-generation solar cells for thin, light, and flexible power conversion devices.[1–6] To achieve the devices with photoconversion efficiencies (PCEs) over 10%, many kinds of polymer and small-molecular materials for the solution-processed OPVs have been reported.[7–15] Because of the good solubility of these materials in solvents, bulk heterojunction (BHJ) structure is dominant for the solution processed OPVs. The supremacy of p–i–n layered structure, in which "i" means the interlayer between p- and n-layers, has been reported for the vacuum deposited OPVs.[16–23] However the solution-processed layer-by-layer structure is difficult to attain, because the lower layer is washed away at the coating of the upper layer.

Recently thermal and photoprecursor approaches have been reported for the construction of solution processed layer-by-layer structures.[24–30] The precursor approach is the way to make insoluble organic semiconductor films by spin-coating of soluble precursors, followed by the quantitative change of the precursors to the insoluble target materials by heating or photoirradiation in situ. Tetrabenzoporphyrin (**BP**) and its metal complexes are one of the best p-type organic semiconducting materials.[31–33] Their films can be prepared by the thermal precursor approach, using bicyclo[2.2.2]octadiene (BCOD)-fused porphyrins (**CP**)[34] or dimethylbicyclo[2.2.2]octadiene (MeBCOD) fused porphyrins (**MeCP**)[35] as soluble precursors. Thin films of **CP** and **MeCP** can be converted to **BP** films by heating at 180–200 ºC. Because of the high crystallinity of **BP**, the **BP** films prepared by this method are polycrystalline with grain sizes of 100 nm scale which is larger than the average exciton diffusion length in organic materials.[36] Because of the good crystallinity, the surface of the **BP** film is rough and the domain sizes of **BP** are larger than the common exciton diffusion length of organic semiconductors.[24]

Recently we have reported fullerene-linked 5-butyl-BP (**Bu-BP–C_{60}**) for the bulk-heterojunction layer to improve the miscibility of p- and n-materials by connecting **BP** and [6,6]-phenyl-C_{61}-butyric acid methyl ester (**PCBM**) with a flexible linker.[37] BHJ device of **Bu-BP–C_{60}** showed a better OPV performance (PCE = 0.15%) than a mixed-layer of **BP** and

[a] Graduate School of Materials Science, Nara Institute of Science and Technology (NAIST), 8916-5 Takayama-cho, Ikoma 630-0192 (Japan)

† Electronic Supplementary Information (ESI) available: [details of synthesis and charactarization of compounds, including ^1H and ^{13}C NMR spectra, cyclic voltammogram and optical data, film preparation, AFM image, XRD pattern and carrier mobilities of the film and OPV device fabrication and OPV performance.]. See DOI: 10.1039/x0xx00000x

PCBM (PCE = 0.02%). Furthermore, the performance of p–i–n device composed of **BP**(p)-, **Bu-BP–C_{60}**(i)- and **PCBM**(n)-layers (PCE = 1.98%) was better than that of the p–i–n device using a mixture of **BP** and **PCBM** for i-layer because of

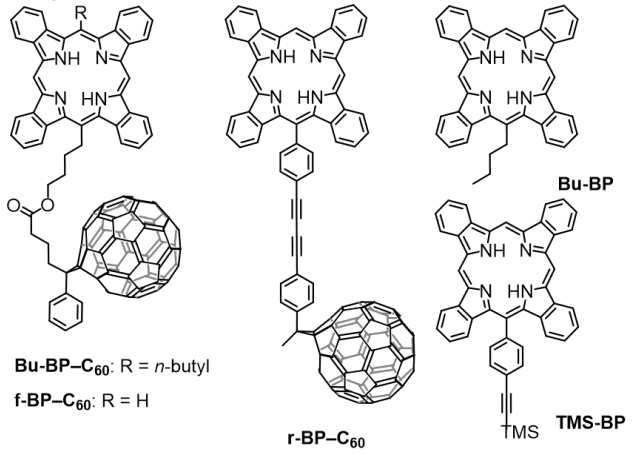

Chart 1. Molecular structures of **Bu-BP–C_{60}**, **f-BP–C_{60}**, **r-BP–C_{60}** and reference compounds (**Bu-BP** and **TMS-BP**).

the better fill factor (FF = 0.60) of the former device than the latter (FF = 0.46). However the performance was still not satisfactory. We hypothesized that the flexible spacer between **BP** and **C_{60}** might accelerate the electron recombination as well as the charge separation between **BP** and **C_{60}**. To verify the hypothesis, we designed mono-substituted **BP–C_{60}** connected by flexible linker (**f-BP–C_{60}**) and rigid linker (**r-BP–C_{60}**) (Chart 1). The butyl group of **Bu-BP–C_{60}** was removed to exclude the effect of insulating alkyl group on **BP**, if any. The carrier mobility and OPV performance of BHJ and p–i–n devices with these materials will be discussed.

For the preparation of **f-BP–C_{60}** and **r-BP–C_{60}**, the effective synthetic procedure of unsymmetrical *meso*-substituted porphyrins is necessary, but it is still limited. Only several synthetic route of mono-*meso*-substituted porphyrins have been reported so far: [2 + 1 + 1] condensation reaction,[38–40] [2 + 2] condensation reaction,[38, 41–44] the reaction of tripyrranes with mono-substituted pyrroles,[38, 45] and the oxidation of pentapyrrane.[46] The yields of the mono–substituted porphyrins were low to moderate. The *meso*-substitution of porphyrin with RLi,[38, 47, 48] the Vilsmeier formylation of copper porphyrin,[49] and chlorination of octaethylporphyrin by *N*-chlorosuccinimide (NCS)[50] also gave mono-*meso*-substituted porphyrins, but the synthesis of 5-substituted porphyrin is still limited. Especially the mono–substituted **BP**s have been hardly reported as far as we know, except a selective halogenation of the precursor **CP** followed by the thermal conversion to **BP.**[50]

Here we will report the synthesis of mono-substituted **CP**s by [2 + 2] and [2 + 1 + 1] condensation reactions in 30-50% yields. The mono-substituted porphyrins were lead to **f-CP–C_{60}** and **r-CP–C_{60}**, the precursors of **f-BP–C_{60}** and **r-BP–C_{60}**, as the materials for the interlayers of the solution-processed three-layered organic photovoltaics.

Results and discussion

A flexible precursor (**f-CP–C_{60}**) of mono-substituted free-base **BP–C_{60}** was prepared as shown in Scheme 1a. The synthetic details are described in Electronic Supplementary Information, ESI†. 5-Substituted **ZnCP 4a** was obtained by [2 + 2] condensation reaction of BCOD-fused dipyrromethane **1**[51] with paraformaldehyde (**2**) and 4-formylbutyric acid methyl ester (**3**)[52], followed by oxidation with chloranil and then zinc insertion. 5-substituted-**ZnCP 4a**, 5,15-disubstituted-**ZnCP 4b**, and non-substituted-**ZnCP** (**ZnCP**) were obtained in 28, 6, and 11% yields, respectively. They were purified by silica-gel column chromatography. The porphyrins **4a**, **4b** and **ZnCP** were obtained as mixtures of stereo-isomers at BCOD moieties. The porphyrin **4a** was converted to flexible free-base **CP–C_{60}** (**f-CP–C_{60}**) following the previously reported procedure: reduction of the ester group to give porphyrin **5**, coupling with [6,6]-Phenyl-C_{61}-butyric acid (**PCBA**)[53] to give **f-ZnCP–C_{60}**, and demetalation by trifluoroacetic acid (TFA) to give **f-CP–C_{60}**. As a reference compound, **5-butyl-CP (Bu-CP)** was prepared using pentanal (**6**) instead of aldehyde **3** followed by demetalation as shown in Scheme 1b.

Next, rigidly-linked **CP–C_{60}** (**r-CP–C_{60}**) was prepared. Since [2 + 2] condensation reaction mentioned above was not successful, [2 + 1 + 1] condensation reaction was tried for aryl-type aldehyde, as shown in Scheme 1c. Because of the low solubility of alkynyl-**CP** derivatives, the MeBCOD-fused pyrrole was used instead of BCOD-pyrrole. By acid condensation of α-hydroxymethylpyrrole **8**,[35] dipyrromethane **9**, and 4-bromoalkynyl-benzaldehyde **10**,[54] 5-substituted-**MeCP 11a** was obtained in 32% yield. The yields of 5,15-disubstituted porphyrin **11b** and non-substituted **MeCP (ZnMeCP)** were only 5% and trace, respectively. 5-Substituted **MeCP 11a** was a mixture of stereoisomers, but was used for the following reactions without further purification. **MeCP 11a** was reacted with fullerene **12**, which was prepared from 4-(trimethylsilylethinyl)acetophenone **17**[55] in 3 steps (See ESI†), to give rigid **r-ZnCP–C_{60}** in 46% yield. Zinc ion of **r-ZnCP–C_{60}** was removed by treatment with TFA to give **r-CP–C_{60}** in 88% yield. In a similar manner, a precursor (**TMS-MeCP**) of the reference compound (**TMS-BP**) was prepared using *p*-[(trimethylsilyl)ethynyl]benzaldehyde **13**[55] instead of benzaldehyde **10** as shown in Scheme 1d. The characterization of the compounds were done by ^{1}H and ^{13}C NMR spectroscopy and high-resolution electrospray ionization (HR-ESI) mass spectroscopy or HR MALDI spiral-TOF mass spectroscopy.

The results of thermogravimetric analysis of **f-CP–C_{60}** and **r-CP–C_{60}** are shown in Figure S1-1 and S1-3, ESI†. The retro-Diels–Alder reaction of **f-CP–C_{60}** started at 120 ºC and finished around 160 ºC, while that of **r-CP–C_{60}** started around 140 ºC and finished around 200 ºC. The observed weight loss of **f-CP–C_{60}** and **r-CP–C_{60}** were 7.19 and 13.25%, which were coincident with the calculated weight loss of 7.13 and 13.34%, respectively. Zinc complex of **r-BP–C_{60}** (**r-ZnBP–C_{60}**) was also prepared for single crystals suitable for the X-ray crystallography. Thermogravimetric analysis of **r-ZnCP–C_{60}** is shown in FigureS1-9, ESI†. The observed weight loss (13.70%) is in MALDI spiral-TOF mass spectra of the obtained **f-BP–C_{60}**, **r-BP–C_{60}** and **r-ZnBP–C_{60}** were in good agreement with

the simulated values (Figure S1-2, 4, 10, ESI†). The retro-Diels–Alder reaction of **f-CP–C$_{60}$** occurred at lower temperature than the rigid ones. After the retro–Diels-Alder reaction, **BP** compounds were thermally stable. The solubility of the **BP–C$_{60}$** compounds was not enough for NMR measurement.

Scheme 1. Synthesis routes of (a) **f-CP–C$_{60}$**, (b) **Bu-CP**, (C) **r-CP–C$_{60}$** and (d) **TMS-CP**.

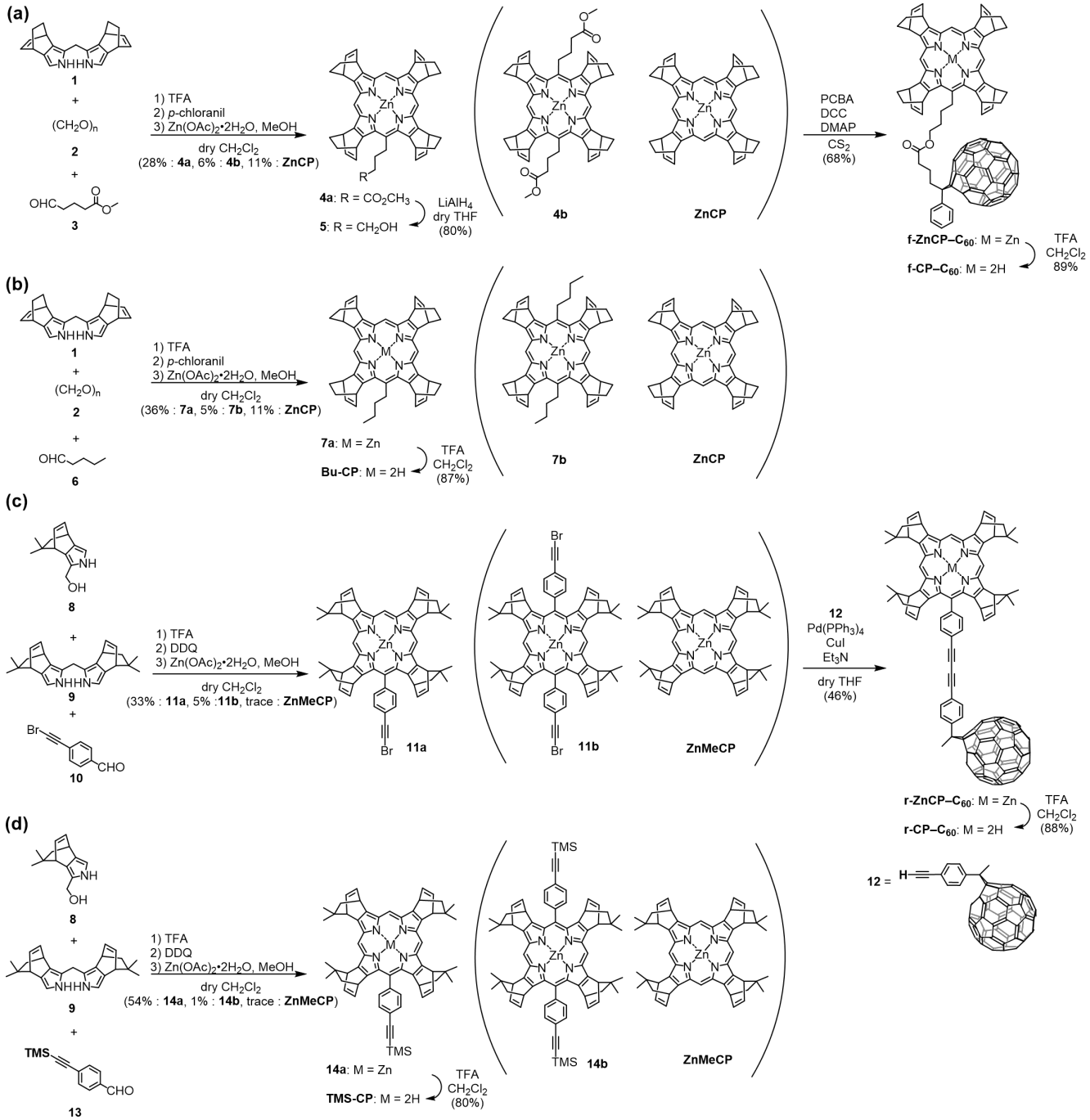

The single crystal structure of **r-ZnBP–C$_{60}$** was determined with synchrotron X-ray radiation (Figure 1, S2, and Table S2, ESI†).[‡, 56, 57] Since the tiny crystals contained many severely disordered solvent molecules in the large void space, they gave only weak diffractions, especially at the high θ range. The molecule is expanded straight and the porphyrin and *meso*-phenyl planes are perpendicular to each other. The porphyrin plane is slightly ruffled. The intramolecular center-to-center distance (d_{cc}) between porphyrin and **C$_{60}$** units is about 22 Å and edge-to-edge distance (d_{ee}) is about 14 Å. In a unit cell, two molecules are placed alternately and the intermolecular distance between porphyrin and **C$_{60}$** units is less than van der Waals distance. This structure is suitable for the effective charge separation but charge recombination is also expected to be fast. The packing structure is shown in Figure S2, ESI†. The top and

side views suggest that fullerenes are arranged in line with the edge-to-edge distance of 3.5 Å, which is suitable for electron transport, while porphyrins are overlapped only at the edge of the benzene rings.

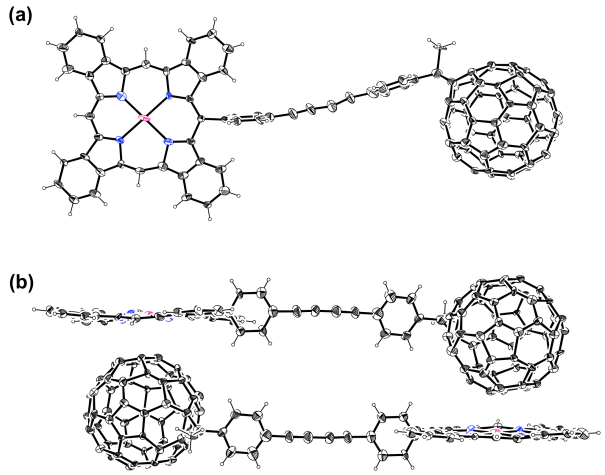

Figure 1. The single crystal structure of **r-ZnBP–C_{60}**. (a) top view and (b) side view with packing structure. The ellipsoids are scaled at 20% probability.

Absorption and fluorescence spectra of **f-BP–C_{60}**, **r-BP–C_{60}** and their reference compounds (**Bu-BP** and **TMS-BP**) are shown in Figure 2a–d and related data are summarized in Table 1. Flexible **f-BP–C_{60}** has a Soret band at 436 nm with a shoulder at 428 nm, Q bands at 568, 609, and 667 nm, and broad absorption of fullerene at 310–350 nm. The absorption peaks are similar to those of the reference **Bu-BP** except for the peaks of fullerene. The solubility of **r-BP–C_{60}** was not enough to obtain the absorption coefficients. The **r-BP–C_{60}** has Soret bands at 419 and 434 nm, Q bands at 568, 601, 608, 664 nm with a shoulder at 615 nm and broad absorption of fullerene at 310–350 nm. The absorption of porphyrin moiety is similar to the reference **TMS-BP**: Soret band at 418 and 433 nm and Q bands at 567, 603, 608, and 664 nm with a shoulder at 615 nm. Due to the lower symmetry of the electronic structure of porphyrin moiety with mono-substituent at 5-position, Soret and Q bands of the porphyrins show the splitting. The absorption band of **f-BP–C_{60}** show the broadening of porphyrin and fullerene peaks compared to the peaks of **r-BP–C_{60}**. The broadening of **f-BP–C_{60}** might come from the intramolecular interaction between **BP** and **C_{60}**.

Fluorescence spectra of **Bu-BP** and **TMS-BP**, the reference **BP**s, showed relatively high fluorescence intensity at 665–666 nm with the fluorescence quantum yields (Φ_f) of 18.5 and 26.6%, respectively. The Φ_f values of dyads, **f-BP–C_{60}** and **r-BP–C_{60}**, in CH_2Cl_2 were 1.0 and 2.5%, respectively. This result suggested that fullerene moieties intramolecularly quench the fluorescence of porphyrins effectively, even though d_{ee} of **r-BP–C_{60}** is 14 Å. The fluorescence lifetimes (τ_f) of **f-BP–C_{60}** and **r-BP–C_{60}** were analyzed in two components: 0.61 ns (96.2%) and 9.38 ns (3.8%) for **f-BP–C_{60}** and 1.16 ns (99.4%) and 11.97 ns (0.6%) for **r-BP–C_{60}**, while those of reference compounds **Bu-BP** and **TMS-BP** were analyzed as single components as 8.74 and 9.91 ns, respectively (Table 1 and Figure S3-1, ESI†). The short lifetimes of **f-BP–C_{60}** and **r-BP–C_{60}** are characterized to intramolecular electron transfer from **BP** to **C_{60}**. Fluorescence lifetimes of **f-BP–C_{60}** were analyzed in two

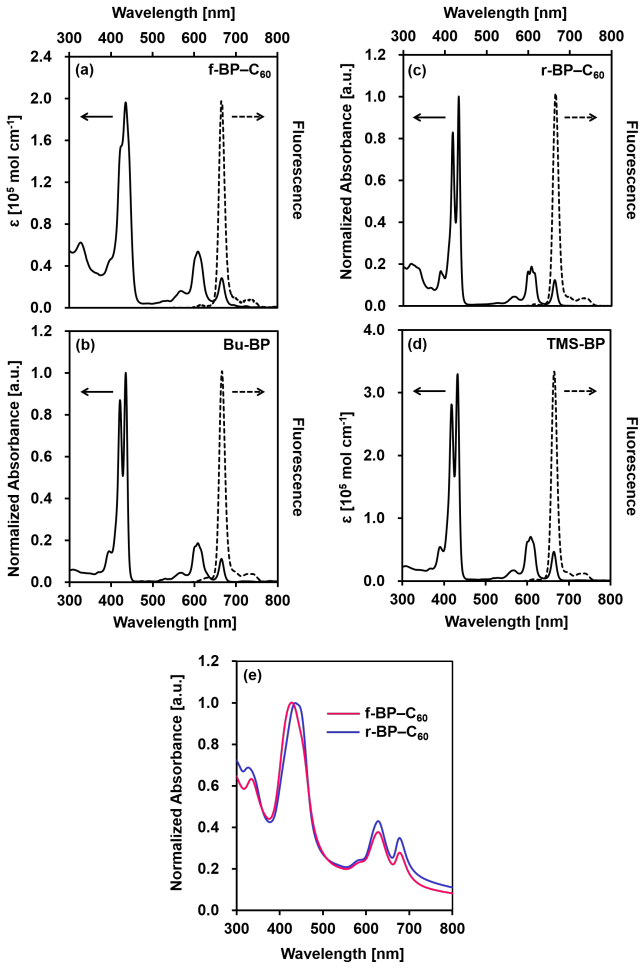

Figure 2. The UV-vis absorption and fluorescence spectra of (a) **f-BP–C_{60}**, (b) **Bu-BP**, (c) **r-BP–C60** and (d) **TMS-BP** in CH_2Cl_2. (e) The UV-vis absorption spectra of **f-BP–C_{60}** and **r-BP–C_{60}** as film. The excitation wavelengths of **f-BP–C_{60}**, **Bu-BP**, **r-BP–C_{60}**, and **TMS-BP** in CH_2Cl_2 are 436, 435, 434, and 433 nm, respectively.

Table 1. Optical properties of fullerene linked **BP**s and reference molecules.

	λ_{abs} [a] [nm]	λ_{abs} [b] [nm]	λ_f [nm]	Φ_f [%]	τ_f [c] [ns] (A)
f-BP–C$_{60}$	327, 428(sh), 436, 568, 609, 667	334, 427, 628, 678	668	1.0	0.61 (96.2) 9.38 (3.8)
Bu-BP	395, 421, 435, 568, 608, 665		665	18.5	8.74
r-BP–C$_{60}$	319, 390, 419, 434, 568, 601, 608, 615(sh), 664	327, 436, 628, 679	668	2.5	1.16 (99.4) 11.97 (0.6)
TMS-BP	391, 418, 433, 567, 603, 608, 615(sh), 664		666	26.6	9.91

[a]In CH_2Cl_2.; [b]As film.; [c]τ_f was measured by excitation at 405 nm in CH_2Cl_2. Emission was monitored at 670 nm.

Table 2. Energy levels and carrier motilities of fullerene linked **BP**s.

	E_g [a] [eV]	HOMO [b] [eV]	LUMO [c] [eV]	μ_h [cm^2 V^{-1} s^{-1}]	μ_e [cm^2 V^{-1} s^{-1}]
f-BP–C$_{60}$	1.6	-5.0	-3.4	2.3×10^{-5}	4.4×10^{-5}
r-BP–C$_{60}$	1.7	-5.1	-3.4	6.8×10^{-5}	5.8×10^{-5}

[a]Determined by the longest absorption edge of the film; [b]Determined by photoelectron spectroscopy in air; [c]LUMO = E_g[a] + HOMO[b].

components as average, although **f-BP–C$_{60}$** could take multiple conformations in solution with flexible linkage. Intramolecular fluorescence quenching of **r-BP–C$_{60}$** (τ_f = 1.16 ns) is not so effective as **f-BP–C$_{60}$** (0.61 ns), because of the rigid spacer with d_{cc} = 22 Å.

The absorption spectra of the **f-BP–C$_{60}$** and **r-BP–C$_{60}$** films are shown in Figures 2e and S3-2, ESI†. The films of **BP–C$_{60}$** were prepared by spin-coating of **CP–C$_{60}$** followed by heating on hotplate at 200 ºC for 20 min. The detail of the film preparation is described in experimental section. The film of **f-BP–C$_{60}$** shows the absorption peaks at 427, 628, and 677 nm, while **r-BP–C$_{60}$** shows at 436, 628, and 677 nm. The spectra of **BP–C$_{60}$** films are broadened compared to the spectra in CH_2Cl_2 because of the π–π stacking of the porphyrins. Q bands peaks of films are similarly red-shifted for **f-BP–C$_{60}$** and **r-BP–C$_{60}$** from those in solution, while Soret band of **r-BP–C$_{60}$** is 9 nm red-shifted than that of **f-BP–C$_{60}$** film.

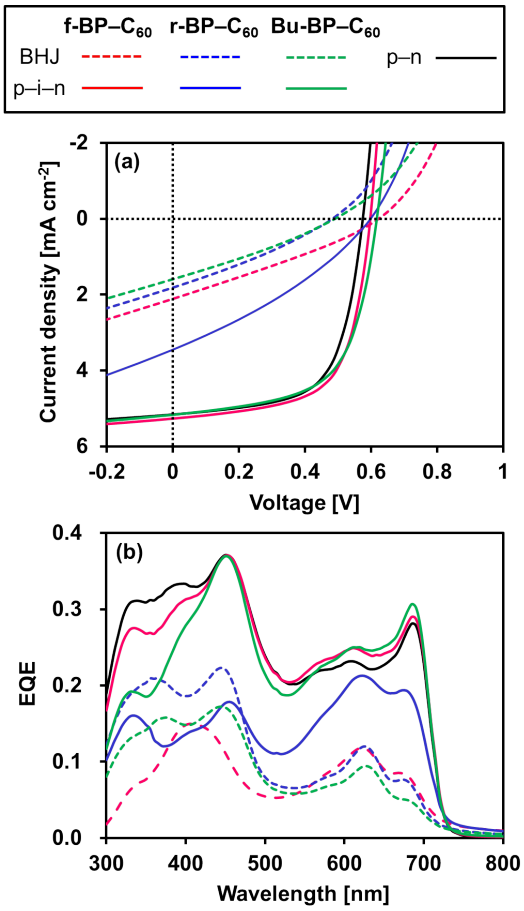

Figure. 3 (a) *J*–*V* curves and (b) EQE spectra of BHJ, p–i–n, and p–n device.

The optical band gap (E_{gap}) obtained by the absorption edge is summarized in Table 2. The highest occupied molecular orbital (HOMO) energies of **f-BP–C$_{60}$** and **r-BP–C$_{60}$** were estimated by photoelectron spectroscopy (PES) of the film in air. The lowest unoccupied molecular orbital (LUMO) energies were estimated from the onset of the cyclic voltammograms (CVs) according to the known empirical equation HOMO = $-E^{ox}_{onset}$ – 4.8 eV, where E^{ox}_{onset} is referenced to the ferrocene/ferrocenium standard. The estimated values are summarized in Table S4, ESI†, with the values of **BP** and **PCBM** films. The HOMO and LUMO energies of the **f-BP–C$_{60}$** and **r-BP–C$_{60}$** films are same although the structures of the linkages between porphyrin and fullerene are different.

To evaluate the electrical properties of the dyads, charge–carrier mobilities of **f-BP–C$_{60}$** and **r-BP–C$_{60}$** films were measured by the space-charge-limited-current (SCLC) technique (Figure S5-1 and Table S5, ESI†). Hole-only devices with the structure of [ITO/MoO_3/**f-BP–C$_{60}$** or **r-BP–C$_{60}$**/MoO_3/Al] and electron-only devices with [ITO/ZnO/**f-BP–C$_{60}$** or **r-BP–C$_{60}$**/LiF/Al] were fabricated. As shown in Table 2, hole and electron mobilities of **f-BP–C$_{60}$** film were 2.3×10^{-5} and 4.4×10^{-5} cm^2 V^{-1} s^{-1}, while those of **r-BP–C$_{60}$** film were 6.8×10^{-5} and 5.8×10^{-5} cm^2 V^{-1} s^{-1}, respectively. The hole and electron mobilities in **f-BP–C$_{60}$** and **r-BP–C$_{60}$** films are roughly balanced, respectively, and seem to be suitable for the BHJ

layer. The hole mobility of **r-BP–C_{60}** is three times larger than that of **f-BP–C_{60}** film, while the electron mobilities of them are almost same to each other.

To evaluate the OPV performances of the BHJ-type devices with [ITO/PEDOT:PSS/**f-BP–C_{60}** or **r-BP–C_{60}** /Ca/Al] structure, **f-BP–C_{60}** or **r-BP–C_{60}** active layer was prepared by spin-coating of **f-CP–C_{60}** or **r-CP–C_{60}** solution followed by heating at 200 ºC for 20 min. The details of the device performance are summarized in Figure S6, ESI† and Experimental. The current density–voltage (*J–V*) curve and external quantum efficiency (EQE) are shown in Figure 3 and the OPV performances are summarized in Table 3. The performance of the previously reported **Bu-BP–C_{60}** was also studied to investigate the influence of additional butyl group at *meso*-position.[35] With the removal of butyl group from **Bu-BP–C_{60}** to **f-BP–C_{60}**, J_{SC} of BHJ device was improved from J_{SC} = 1.60 mA cm^{-2} to 1.82 mA cm^{-2} with the improvement of series resistance (R_S), while V_{OC} and FF did not change (Table 3 and S6, ESI†). PCE was almost same as 0.23 and 0.26 % of **f-BP–C_{60}** and **Bu-BP–C_{60}**,

Table 3. Device performances

Device type	i-layer	J_{SC}[a] [mA cm^{-2}]	V_{OC}[a] [V]	FF[a]	best PCE[a] [%]	average PCE[b] [%]
BHJ	**f-BP–C_{60}**	1.82	0.48	0.29	0.26	0.26±0.00
	r-BP–C_{60}	2.11	0.62	0.29	0.38	0.35±0.03
	Bu-BP–C_{60}[c]	1.60	0.49	0.29	0.23	0.22±0.01
p–i–n	**f-BP–C_{60}**	5.27	0.60	0.63	2.00	1.97±0.03
	r-BP–C_{60}	3.46	0.60	0.32	0.67	0.66±0.01
	Bu-BP–C_{60}[c]	5.17	0.62	0.61	1.93	1.91±0.02
p–n	–	5.16	0.57	0.64	1.89	1.78±0.10

[a]According to the best value of the device.; [b]Four device in all.; [c]Device performances were slightly different to our previous report,[37] because different device structure was applied for comparison with **f-BP–C_{60}** and **r-BP–C_{60}**.

Table 4. Effect of i-layer condition for p–i–n devices **f-BP–C_{60}**.

Thickness of i-layer [nm]	J_{SC} [mA cm^{-2}]	V_{OC} [V]	FF	PCE [%]	R_S [Ω cm^2]	R_{sh} [Ω cm^2]
46	5.26	0.59	0.59	1.82	9	650
45	5.15	0.61	0.60	1.91	12	1101
41	5.23	0.59	0.63	1.93	10	1092
39	5.28	0.58	0.65	1.98	7	1335
35	5.27	0.60	0.63	2.00	8	1254
30	4.94	0.57	0.64	1.81	6	1189

respectively. This result suggests butyl group at *meso*-position little influence the OPV performance. With the rigid linker, **r-BP–C_{60}** showed better J_{SC} and V_{OC}, which improved the PCE to 0.38%. These results are in good agreement with SCLC performance, where **r-BP–C_{60}** film has better carrier mobility than **f-BP–C_{60}** film.

The microscopic surface morphology of the films was investigated by tapping-mode atomic-force microscopy (AFM), as shown in Figures 4a and 4b. Both of the **f-BP–C_{60}** and **r-BP–C_{60}** films showed relatively smooth surface with root-mean square (RMS) roughness of 0.41 and 0.81 nm. The crystallinity of the films was examined by out-of-plane X-ray diffraction (XRD) analysis, but no signal peaks were observed (Figure S5-2, ESI†), which suggested the films are amorphous. The annealing temperature was change from 160 to 220 ºC, but results were same. Although **r-BP–C_{60}** film has better carrier mobility than **f-BP–C_{60}** film, we could not find the apparent difference on film morphology of these films.

Next the p–i–n devices were prepared by sequential fabrication of the **BP**-, **BP–C_{60}**- and **PCBM**-layers as p-, i-, and n-layers, respectively (Fig S6, ESI†). The *J–V* curves and EQE spectra are shown in Figure 3 and the data is summarized in Table 3 with those of p–n device using **BP** and **PCBM** as a reference. The optimization of the film thickness of i-layers are summarized in Table 4 and 5, while p-layer and n-layer were fixed to 23 and 45 nm, respectively.[37] With **f-BP–C_{60}** for i-layer, the film thickness of i–layer was changed from 46 to 30 nm, and the best PCE performance of p–i–n device was obtained as J_{SC} = 5.27 mA cm^{-2}, V_{OC} = 0.60 V, FF = 0.63 and PCE = 2.00%, at 35 nm thickness. The performance is comparable with that of **Bu-BP–C_{60}**, and the removal of butyl group on *meso*-position of **BP** did not affect the PCE performance of p–i–n device apparently. For p–i–n device using **r-BP–C_{60}**, J_{SC} and FF were not so improved from BHJ device and the best PCE was only 0.67% at 46 nm thickness of i-layer. It is interesting that the PCE performance of BHJ device for **r-BP–C_{60}** is better, while that of p–i–n device was worse than **f-BP–C_{60}**. The OPV performance of p–i–n with **f-BP–C_{60}** for i–layer was only slightly improved from p–n device of **BP** and **PCBM**.

To investigate the morphology of the i-layer, AFM image of i-layers on p-layer (**BP** film) was measured. The AFM of **BP** film is shown in Figure S5-3, ESI†[37]. The RMS roughness is relatively high as 12.4 nm because of the high crystallinity of **BP**. The RMS roughness of **f-BP–C_{60}** films on **BP** layer is 4.88 nm, while RMS of **r-BP–C_{60}** on **BP** layer is 7.75 nm (Figure 4c and 4d). The flexible

Table 5. Effect of i-layer condition for p–i–n devices **r-BP–C_{60}**.

Thickness of i-layer [nm]	J_{SC} [mA cm^{-2}]	V_{OC} [V]	FF	PCE [%]	R_S [Ω cm^2]	R_{sh} [Ω cm^2]
50	2.20	0.62	0.31	0.42	148	423
46	3.46	0.60	0.32	0.67	72	280
43	2.63	0.57	0.32	0.48	107	340
39	2.35	0.59	0.31	0.42	138	363
38	2.32	0.40	0.28	0.26	136	204
34	2.19	0.26	0.26	0.15	108	129

f-BP–C_{60} can level and smooth the rough p-layer surface, but rigid **r-BP–C_{60}** could not offset the roughness of the lower layer. The surface of the n-layers on i-layers shows similar

AFM images for the three devices and the RMS roughness of the **PCBM** layers on **f-BP–C_{60}**, and **r-BP–C_{60}** layers are 1.73 and 1.08 nm, respectively (Figure S5-3, ESI†). The similarity of the roughness of the two systems seems to come from the amorphous property of **PCBM**. Thus rigid

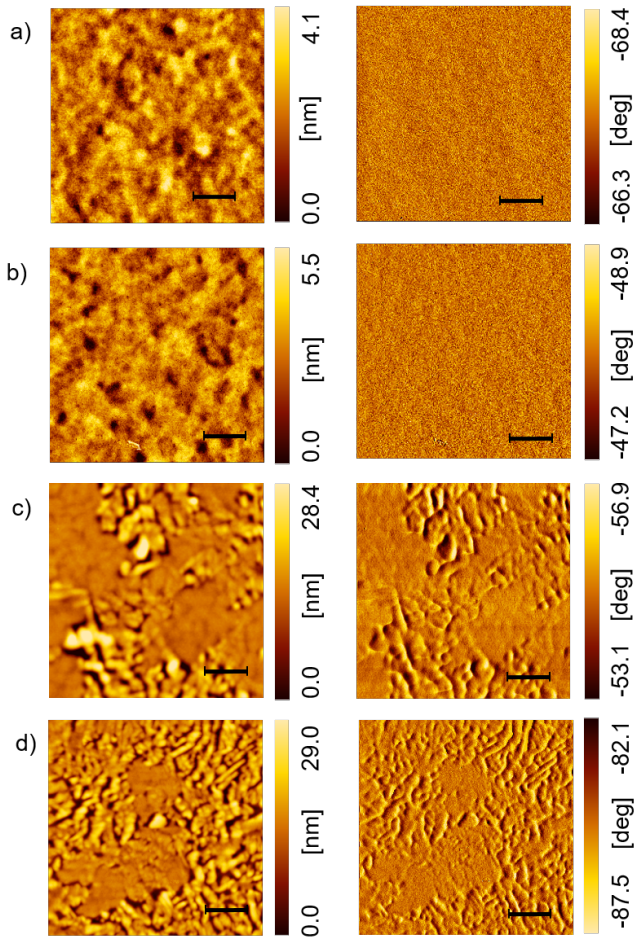

Figure 4. Tapping-mode AFM height (left) and phase (right) images. Single layer of a) **f-BP–C_{60}** film and b) **r-BP–C_{60}** on PEDOT:PSS/ITO glass substrate. Layered film of c) **f-BP–C_{60}** and d) **r-BP–C_{60}** on **BP**-layer. RMS values are 0.41, 0.81, 4.48 and 7.75 nm, respectively. The scale bars correspond to 1 μm.

r-BP–C_{60} layer on **BP** layer does not have good interface morphology, while **f- BP–C_{60}** could even the surface of the p-layer because of the flexibility. Since the **r-BP–C_{60}** is rigid and could not smooth the roughness of p-layer as shown in AFM image, the rigid structure might have a worse effect on the carrier injection between p-layer and i-layer. Since the mobility of **r-BP–C_{60}** film is higher than that of **f-BP–C_{60}**, the combination with smooth p-layer might improve the performance. The p–n device of **BP** and **PCBM** showed relatively high performance, which was almost comparable to p–i–n structure with **f-BP–C_{60}**. This is because the rough surface of **BP** was covered with amorphous **PCBM** and the pseudo-p–i–n structure was constructed in p–n device.[24]

Conclusions

We were successful to establish the synthetic method for 5-subsituted **BP**s in moderate yields and have prepared mono-substituted **BP–C_{60}** compounds connected by flexible and rigid linkers: **f-BP–C_{60}** and **r-BP–C_{60}**. The fluorescence of **BP** was quenched more efficiently for **f-BP–C_{60}** than for **r-BP–C_{60}** in CH_2Cl_2 because of the intramolecular through-space approach of **C_{60}** to **BP** by flexible spacer. In the film, **r-BP–C_{60}** showed higher hole and electron carrier mobilities than **f-BP–C_{60}**. The well-balanced carrier mobility of **r-BP–C_{60}** film resulted in the twice better performance of BHJ-type OPV than **f-BP–C_{60}**. However, when the molecules are used for i-layers of p–i–n devices, the trend was reversed. The OPV performance of p–i–n device with **f-BP–C_{60}** in i-layer was 2.0%, while that with **r-BP–C_{60}** was 0.67%. The flexible structure of **f-BP–C_{60}** smoothed the rough surface of p-layer and kept the good FF of p–n device even in the p–i–n device, while the FF of p–i–n with **r-BP–C_{60}** was depressed to 0.32. The rigid and long molecule might be not suitable to smooth the interface on high-roughness p-layer.

As mentioned above, the interface of the p–n device with **BP** and **PCBM** is rough and therefore it will take intrinsically pseudo p–i–n structure with crystalline **BP**-layer and amorphous **PCBM**-layer. To improve the p–n device of **BP** and **PCBM** by p–i–n structure using **BP–C_{60}** dyad for i-layer, p- and n-materials in i-layer should be well-mixed and interface area of p- and n-materials has to be spread for the effective charge separation. This result suggests that proper crystallinity gives the better carrier mobilities, but at the same time, smooth interface between each layer is required. For the better charge separation, short face-to-edge distance between **BP** and **C_{60}** is necessary and for the better charge transport, appropriate rigidity, but not expanded shape, might be desirable. Considering these points, the linkers to keep **C_{60}** on **BP** plane might be suitable. Synthesis of the next-generation donor-acceptor compounds is undergoing.

Experimental

Synthesis and structural characterization of compounds

General. Anhydrous THF (Super Plus grade, stabilizer free) and CH_2Cl_2 (Super grade) were obtained from Kanto Chemical and used as received. All the other solvents and chemicals were of reagent grade obtained commercially and used without further purification. Room temperature, or rt, means 20–25 °C. Material purifications were performed by column chromatography on Silica Gel 60N (Kanto Chemical Co.) and by gel permeation chromatography (GPC) was conducted with a JAI LC-9225NEXT (JAIGEL-2H-40/JAIGEL-1H-40) at room temperature using $CHCl_3$ as a eluent. ^{1}H NMR and $^{13}C\{^1H\}$ NMR spectra were recorded on a JNM-ECX400 spectrometer using tetramethylsilane or solvent as an internal standard. ESI and MALDI-TOF mass spectra were measured on a JEOL JMS-T100LC AccuTOF spectrometer and JEOL spiral TOF JMS-S3000 spectrometer, respectively.

Thermal reaction profiles. The thermogravimetric analysis (TGA) was carried out on a Seiko Exstar 6000 TG/DTA 6200 instrument under nitrogen gas flow with a heating rate of 5 °C min^{-1}. Materials converted by heating (200 ºC, 10 min) were

investigated by MALDI-TOF mass spectra measured on a JEOL spiral TOF JMS-S3000 spectrometer.

X-ray crystal structure. Single-crystal diffraction analysis data collection was carried out at low temperature (90 K) on a Rigaku Saturn 724 diffractometer using synchrotron radiation and a large cylindrical imaging plate camera at SPring-8 beam line BL40XU (Hyogo, Japan), (proposal No. 2015A1388).

Optical properties. UV-vis spectra were measured on a JASCO UV/VIS/NIR Spectro-photometer V-570. Steady-state fluorescence spectra were measured on JASCO FP-6600 in the range of 300-800 nm. For spectral measurements as a solution, spectral grade CH_2Cl_2 was purchased from Nacalai tesque Inc. Fluorescence quantum yields were measured on an Absolute PL Quantum Yield Measurement System C9920-02. Fluorescence lifetimes were measured on C4780 picosecond fluorescence lifetime measurement device (Hamamatsu Photonics). A Mira Model 900-F & Pulse Switch femtosecond pulse laser was used, and the excitation light wave length was 405 nm from Coherent Verdi V-5 Nd:YVO_4 laser.

Cyclic voltammetry (CV) and differential pulse voltammetry (DPV). CV measurements were conducted in a solution of 0.1 M $TBAPF_6$ in dry benzonitrile with a scan rate of 100 mV/s at room temperature in an argon-filled cell. A glassy carbon electrode and a Pt wire were used as a working and a counter electrode, respectively. An Ag/Ag^+ electrode was used as reference electrode, which was normalized with the half-wave potential of ferrocene/ferrocenium$^+$ (Fc/Fc^+) redox couple. The DPV measurements were performed under same condition as the CV measurements. The HOMO/LUMO energy levels were determined from the onset oxidation potential (HOMO = – (4.8 + E^{onset}_{ox})) and reduction potential (LUMO = – (4.8 + E_{onset}^{red})), where the reference electrode (vs. Fc/Fc+) relative to vacuum is taken to be 4.8 eV.

Characterization of film properties

Film preparation. The typical film of **f-BP–C_{60}** or **r-BP–C_{60}** were prepared on clean ITO/glass substrates. The spin coating of a 10 mg mL^{-1} solution of **f-CP–C_{60}** or **r-CP–C_{60}** in chloroform at 1000 rpm for 30 s followed by heating at 200 ºC for 20 min gave **f-BP–C_{60}** or **r-BP–C_{60}** films. The spin coating and heating were done in a nitrogen-filled glovebox. The absorption spectra of **f-CP–C_{60}** and **r-CP–C_{60}** are summarized in Figure S3-2.

Film Thickness. Film thickness was measured by Surface Profiler ET200 (Kosaka Laboratory Ltd.). The value was obtained as an average of 10 measurement points.

Estimation of energy level. Ionization potential of the films was measured by a Riken photoelectron spectroscopy instrument, AC-3. The obtained ionization energies (Figs. S4-1) are used to approximate HOMO levels of the materials in the thin-film state.

Atomic force microscope (AFM) measurement. The surface morphology of organic films was observed by SPA400, SPI3800N AFM (Seiko instruments Inc.) in tapping mode using silicon probes with a resonant frequency of ~138 kHz and a force constant of 16 N m^{-1}.

X-ray diffraction (XRD) measurements. The bulk structure of thin-films was evaluated by out-of-plane XRD measurements using a RINT-TTRIII/NM diffractometer equipped with a rotating anode (Cu Kα radiation, λ = 1.5418 Å). The sample films were prepared as described above on clean ITO glass without PEDOT:PSS.

Space-charge-limited-current (SCLC) measurement. Charge-carrier mobilities in **f-BP–C_{60}**, **r-BP–C_{60}** and **Bu-BP–C_{60}** films were evaluated by the SCLC method using an Agilent HP4155C semiconductor parameter analyzer. The SCLC device structures for hole-only and electron-only measurements were ITO/MoO_3/active layer/MoO_3/Al and ITO/ZnO/active layer/LiF/Al, respectively. Each active layer was prepared by spin coating of **f-CP–C_{60}**, **r-CP–C_{60}** and **Bu-CP–C_{60}** in chloroform (14 mg/mL) at 800 rpm for 30 seconds on ITO/MoO_3 (15 nm) or ITO/ZnO (28 nm), respectively. After spin-coating, these films were heated in the same condition for the OPV device fabrication to convert to **f-BP–C_{60}**, **r-BP–C_{60}** and **Bu-BP–C_{60}** in the nitrogen-filled glove box. After preparation of the organic layers, MoO_3 (15 nm) / Al (50 nm) and LiF (1 nm) / Al (50 nm) were vapor deposited at high vacuum (< 5.0×10^{-4} Pa), respectively.

OPV Device fabrication and photovoltaic performance

Device fabrication. Indium-tin-oxide (ITO)-patterned glass substrates (20.0 × 25.0 mm, 15 Ω per square) were washed with running water and were ultrasonically cleaned in detergent, pure-water and isopropanol for 10 min each. After the substrates were dried, (3,4-ethylenedioxythiophene):poly(4-styrenesulfonate) (PEDOT:PSS, Clevios P VP AI4083) was spin coated (3000 rpm, 30 sec) in air followed by a thermal annealing treatment at 130 °C for 10 min in air. The thickness of the resulting PEDOT:PSS layer was about 30 nm. The substrates were transferred to a N_2-filled glove box (<10.0 ppm O_2 and H_2O). The deposition process of organic active layers is illustrated in Fig. S1. The active layers for BHJ device were deposited by spin coating of a chloroform solution (10 mg/mL, 1500 rpm, 30 sec) of **f-CP–C_{60}** or **r-CP–C_{60}** followed by heating (180 ºC, 20 min) for in-situ conversion to **f-BP–C_{60}** or **r-BP–C_{60}**. To fabricate p–i–n device, the p-layer was prepared by spin-coating of a chloroform solution (7 mg/mL, 2500 rpm, 30 sec) of **CP** followed by heating (200 ºC, 20 min) to effect the in-situ conversion of **CP** to **BP**. The film thickness was about 23 nm. The most effective i-layers were deposited by spin coating (1500 rpm, 30 sec) of a chloroform solution of **f-CP–C_{60}** (7 mg/mL) or **r-CP–C_{60}** (10 mg/mL) followed by heating (200 ºC, 20 min) to effective in-situ conversion to **f-BP–C_{60}** or **r-BP–C_{60}** as shown in Table 4 and 5. The n-layer was prepared by spin-coating of a chloroform solution of **$PC_{61}BM$** (7 mg/mL, 1500 rpm, 30 s) and annealed (195 ºC, 20 min). The film thickness was about 45 nm. After preparation of the organic layers, buffer layer (Ca, 5 nm) and counter electrode (Al, 50 nm) were vapor deposited at high vacuum (<5.0×10^{-4} Pa) through a shadow mask that defined an active area to 4 mm^2.

OPV performances. Current–voltage (*J–V*) curves were measured using a Keithley 2611B SYSTEM Source Mater unit under AM1.5G illumination at an intensity of 100 mW cm–2

using a solar simulator (Bunko-keiki, CEP-2000RP). The external quantum efficiency (EQE) spectra were obtained under illumination of monochromatic light using the same system

Acknowledgements

This work was partly supported by CREST, JST, Grants-in-Aid for Scientific Research (Nos. 25288092, 26620167, 26105004, and 16H02286), Grant-in-Aid for JSPS Research Fellow, the Green Photonics Project in NAIST, and the program for promoting the enhancement of research universities in NAIST supported by MEXT. We thank The Nippon Synthetic Chemical Industry Co., Ltd. (Osaka, Japan) for the supply of ethyl isocyanoacetate, a starting material for the synthesis of **BP**s. We thank Ms. Y. Nishikawa and Mr. Y. Okazima (NAIST) for the mass spectroscopy and the fluorescence lifetime, respectively. Single-crystal X-ray analysis was performed at BL40XU of SPring-8 with the approval of the Japan Synchrotron Radiation Research Institute (JASRI; 2015A1388). We thank Dr. Nobuhiro Yasuda (JASRI), Prof. Hikaru Takaya, and Dr. Takahiro Iwamoto (Kyoto University) for their guidance for X-ray crystallographic analysis and for valuable discussions.

Notes and references

‡ CCDC number for the crystal structure of **r-ZnBP–C_{60}** is 1496658.

1 C. J. Brabec, N. S. Sariciftci and J. C. Hummelen, *Adv. Funct. Mater.*, 2001, **11**, 15.
2 K. M. Coakley and M. D. McGehee, *Chem. Mater.*, 2004, **16**, 4533.
3 P. M. Beaujuge and J. M. J. Fréchet, *J. Am. Chem. Soc.*, 2011, **133**, 20009.
4 M. Kaltenbrunner, M. S. White, E. D. Głowacki, T. Sekitani, T. Someya, N. S. Sariciftci and S. Bauer, *Nat. Commun.*, 2012, **3**, 770.
5 G. Li, R. Zhu and Y. Yang, *Nat. Photonics*, 2012, **6**, 153.
6 L. Dou, J. You, Z. Hong, Z. Xu, G. Li, R. A. Street and Y. Yang, *Adv. Mater*, 2013, **25**, 6642.
7 C.-C. Chen, W.-H. Chang, K. Yoshimura, K. Ohya, J. You, J. Gao, Z. Hong, and Y. Yang, *Adv. Mater.*, 2014, **26**, 5670.
8 Y. Liu, J. Zhao, Z. Li, C. Mu, W. Ma, H. Hu, K. Jiang, H. Lin, H. Ade and H. Yan, *Nat. Commun.*, 2014, **5**, 529.
9 S.-H. Liao, H.-J. Jhuo, P.-N. Yeh, Y.-S. Cheng, Y.-L. Li, Y.-H. Lee, S. Sharma and S.-A. Chen, *Sci. Rep.*, 2014, **4**, 6813.
10 A. R. bin M. Yusoff, D. Kim, H. P. Kim, F. K. Shneider, W. J. da Silva and J. Jang, *Energy Environ. Sci.*, 2015, **8**, 303.
11 J.-D. Chen, C. Cui, Y.-Q. Li, L. Zhou, Q.-D. Ou, C. Li, Y. Li and J.-X. Tang, *Adv. Mater.*, 2015, **27**, 1035.
12 B. Kan, M. Li, Q. Zhang, F. Liu, X. Wan, Y. Wang, W. Ni, G. Long, X. Yang, H. Feng, Y. Zuo, M. Zhang, F. Huang, Y. Cao, T. P. Russell and Y. Chen, *J. Am. Chem. Soc.*, 2015, **137**, 3886.
13 Z. He, B. Xiao, F. Liu, H Wu, Y. Yang, S. Xiao, C. Wang, T. P. Russell and Y. Cao, *Nat. Photonics*, 2015, **9**, 174.
14 V. Vohra, K. Kawashima, T. Kakara, T. Koganezawa, I. Osaka, K. Takimiya and H. Murata, *Nat. Photonics*, 2015, **9**, 403.
15 Z. Wu, C. Sun, S. Dong, X.-F. Jiang, S. Wu, H. Wu, H.-L. Yip, F. Huang and Y Cao, *J. Am. Chem. Soc.*, 2016, **138**, 2004.
16 M. Hiramoto, H. Fujiwara and M. Yokoyama, *Appl. Phys. Lett.* 1991, **58**, 1062.
17 M. Hiramoto, H. Fujiwara and M. Yokoyama, *Appl. Phys. Lett.* 1992, **72**, 3781.
18 J. Drechsel, B. Männig, F. Kozlowski, D. Gebeyehu, A. Werner, M. Koch, K. Leo and M. Pfeiffer, *Thin Solid Films*, 2004, **451-452**, 515.
19 T. Taima, M. Chikamatsu, Y. Yoshida, K. Saito and K. Yase, *Appl. Phys. Lett.*, 2004, **85**, 6412.
20 J. Drechsel, B. Männig, F. Kozlowski, M. Pfeiffer, K. Leo and H. Hoppe, *Appl. Phys. Lett.*, 2005, **86**, 244102.
21 M. Hiramoto and K. Sakai, *Proc. SPIE,* 2008, **7052**, 70520H.
22 W. Tress, K. Leo and M. Riede, *Solar Energy Mater. Solar Cells*, 2011, **95**, 2981.
23 E. Siebert-Henze, V. G. Lyssenko, J. Fischer, M. Tietze, R. Brueckner, T. Menke, K. Leo and M. Riede, *Org. Electronics*, 2014, **15**, 563.
24 Y. Matsuo, Y. Sato, T. Niinomi, I. Soga, H. Tanaka, and E. Nakamura, *J. Am. Chem. Soc.*, 2009, **131**, 16048.
25 Y. Zhen, H. Tanaka, K. Harano, S. Okada, Y. Matsuo and E. Nakamura, *J. Am. Chem. Soc.,* 2015, **137**, 2247.
26 S.-Y. Ku, C. D. Liman, J. E. Cochran, M F. Toney, M. L. Chabinyc and C. J. Hawker, *Adv. Mater.*, 2011, **23**, 2289.
27 H. Tanaka, Y. Abe, Y. Matsuo, J. Kawai, I. Soga, Y. Sato and E. Nakamura, *Adv. Mater.*, 2012, **24**, 3521.
28 H. Yamada, Y. Yamaguchi, R. Katoh, T. Motoyama, T. Aotake, D. Kuzuhara, M. Suzuki, T. Okujima, H. Uno, N. Aratani and K. Nakayama, *Chem. Commun*. 2013, **49**, 11638.
29 H. Saeki, O. Kurimoto, H. Nakaoka, M. Misaki, D. Kuzuhara, H. Yamada, K. Ishida and Y. Ueda, *J. Mater. Chem. C*, 2014, **2**, 5357.
30 Y. Yamaguchi, M. Suzuki, T. Motoyama, S. Sugii, C. Katagiri, K. Takahira, S. Ikeda, H. Yamada and K. Nakayama, *Sci. Rep.*, 2014, **4**, 7151.
31 P. B. Shea, J. Kanicki, L. R. Pattison, P. Petroff, M. Kawano, H. Yamada and N. Ono, *J. Appl. Phys.*, 2006, **100**, 034502.
32 P. B. Shea, L. R. Pattison, M. Kawano, C. Chen, J. Chen, P. Petroff, D. C. Martin, H. Yamada, N. Ono and J. Kanicki, *Synth. Metals*, 2007, **157**, 190.
33 P. B. Shea, H. Yamada, N. Ono and J. Kanicki, *Thin Solid Films*, 2012, **520**, 4031.
34 S. Ito, T. Murashima, H. Uno and N. Ono, *Chem. Commun.* 1998, 1661.
35 T. Okujima, Y. Hashimoto, G. Jin, H. Yamada, H. Uno, and N. Ono, *Tetrahedron*, 2008, **64**, 2405.
36 O. V. Mikhnenko, P. W. M. Blom and T.-Q. Nguyen, *Energy Environ. Sci.*, 2015, **8**, 1867.
37 Y. Tamura, H. Saeki, J. Hashizume, Y. Okazaki, D. Kuzuhara, M. Suzuki, N. Aratani and H. Yamada, *Chem. Commun.*, 2014, **50**, 10379.
38 M. O. Senge, Y. M. Shaker, M. Pintea, C. Ryppa, S. S. Hatscher, A. Ryan and Y. Sergeeva., *Eur. J. Org. Chem.*, **2010**, 237.
39 A. Wiehe, C. Ryppa, and M. O. Senge, *Org. Lett*. 2002, **4**, 3807.
40 C. Ryppa, M. O. Senge, S. S. Hatscher, E. Kleinpeter, P. Wacker, U. Schilde and A. Wiehe, *Chem. Eur. J.*, 2005, **11**, 3427.
41 D. K. Dogutan, M. Ptaszek and J. S. Lindsey, *J. Org. Chem.*, 2008, **73**, 6187.
42 D. Fan, M. Taniguchi, Z. Yao, S. Dhanalekshmi and J. S. Lindsey, *Tetrahedron*, 2005, **61** 10291.
43 G. B. Rowland, K. Barnett, J. I. DuPont, G. Akurathi, V. H. Le and E. A. Lewis, *Bioorg. Med. Chem.*, 2013, **21**, 7515.
44 F. L. Otte, S. Lemke, C. Schütt, N. R. Krekiehn, U. Jung, O. M. Magnussen and R. Herges, *J. Am. Chem. Soc.*, 2014, **136**, 11248.
45 I. Saltsman, I. Goldberg, Y. Balasz and Z. Gross, *Tetrahedron Lett.*, 2007, **48**, 239.
46 I. Saltsman and Z. Gross, *Tetrahedron Lett.*, 2008, **49**, 247.
47 X. Feng, I. Bischoff, and M. O. Senge, *J. Org. Chem*., 2001, **66**, 8693.
48 M. O. Senge, Acc. *Chem. Res*. 2005, **38**, 733.
49 P. P. Liu, Y. Q. Feng, C. Z. Gu, S. X. Meng and B. Zhang, *Chin. Chem. Lett.,* 2012, **23**, 505.

50 S. Ito, L. T. Phong, T. Komatsu, N. Igarashi, S. Otsubo, Y. Sakai, A. Ohno, S. Aramaki, Y. Tanaka, H. Uno, T. Oba and K. Hiratani, *Eur. J. Org. Chem.*, 2009, 5373.
51 H. Yamada, K. Kushibe, T. Okujima, H. Uno and N. Ono, *Chem Commun.*, 2006, 383.
52 V. Hickmann, A. Kondoh, B. Gabor, M. Alcarazo and A. Fürstner, *J. Am. Chem. Soc.* 2011, **133**, 13471.
53 T. Nishizawa, K. Tajima and K. Hashimoto, *J. Mater. Chem.*, 2007, **17**, 2440.
54 C. B. Aakeröy, A. S. Sinha, K. N. Epa, C. L. Spartz and J. Desper, *Chem. Commn.*, 2012, **48**, 11289.
55 S. Thorand and N. Krause, *J. Org. Chem.*, 1998, **63**, 8551.
56 N. Yasuda, H. Murayama, Y. Fukuyama, J. Kim, S. Kimura, K. Toriumi, Y. Tanaka, Y. Moritomo, Y. Kuroiwa, K. Kato, H. Tanaka and M. Takata, *J. Synchrotron Rad.*, 2009, **16**, 352.
57 N. Yasuda, Y. Fukuyama, K. Toriumi, S. Kimura and M. Takata, *AIP Conference Proceedings*, 2010, **1234**, 147.

